Supplementary Figures

Supplementary Figure 1. In vitro fit and direct statistical analysis of the xenograft breast data (LM2-4^{luc+})

Supplementary Figure 2. Population fit of the tumor growth data that were measured by BL, under the Gomp-Exp model and initial volume V_i fixed by the conversion rule inferred from the correlation between volume and BL (1 cell $\simeq 10$ p/s, 10^6 cells injected at day 0)

Supplementary Figure 3. Population fits of the breast xenograft data under different growth theories

Supplementary Figure 4. Population fits of the kidney isograft data under different growth theories

Supplementary Figure 5. Second kidney data set used for fitting the data (resection time = 23 days)

Supplementary Figure 6. Individual fits of primary tumor and metastatic burden kinetics. Breast animal model

Supplementary Figure 7. Individual fits of primary tumor and metastatic burden kinetics. Kidney animal model

Supplementary Figure 8. Link between experimental and model survival

Supplementary Figure 9: Surgery benefit on survival and metastatic burden reduction as a function of resection size, for varying values of metastatic potential (parameter μ)

Supplementary Figure 10. Population fits of the ortho-surgical metastasis animal models for a dissemination coefficient $\mathrm{d}(\mathbf{V_p}) = \mu \mathbf{V_p^\gamma}$ and various values of γ

Supplementary Figure 11. Population fits of the ortho-surgical metastasis animal models for various values of the signal-to-cell ratio V_0

Supplementary Movie 1: Simulation of the cancer history from the first cancer cell for a virtual patient with median μ

Supplementary Movie 2: Simulation of the cancer history from the first cancer cell for a virtual patient with large μ, at the 90th percentile.

Supplementary Figure 1. In vitro fit and direct statistical analysis of the xenograft breast data (LM2-4^{luc+})

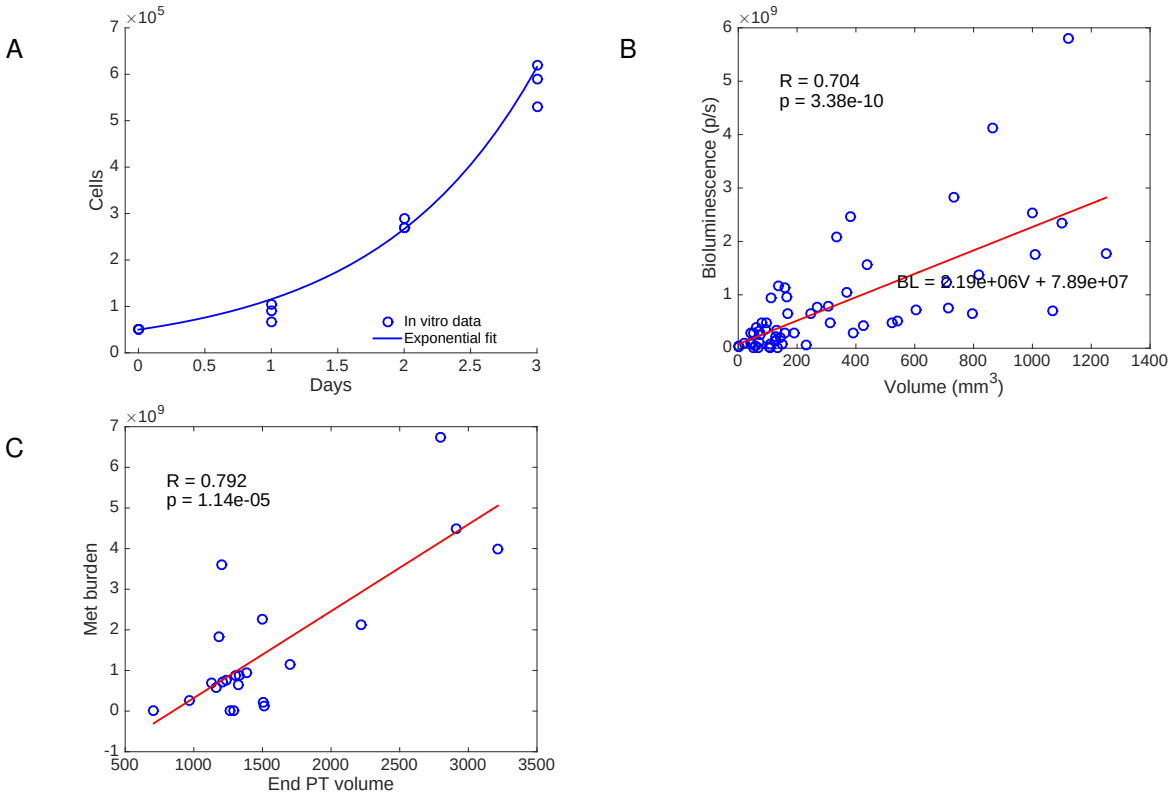

A. *In vitro* proliferation kinetics and exponential fit of the LM2-4^{luc+} cell line. Three replicates
B. Correlation between bioluminescence emission and caliper-measured volume of the primary tumor
C. Correlation between PT volume at resection and final metastatic burden
PT = Primary Tumor

Supplementary Figure 2. Population fit of the tumor growth data that were measured by BL, under the Gomp-Exp model and initial volume V_i fixed by the conversion rule inferred from the correlation between volume and BL (1 cell $\simeq 10$ p/s, 10^6 cells injected at day 0)

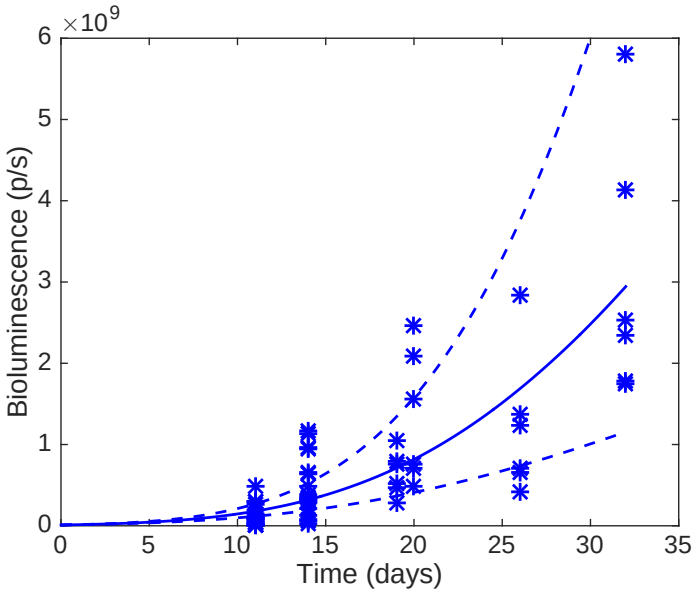

Fit was performed using nonlinear mixed effects modeling (function *nlmefitsa* of Matlab). Plain line is the median output from the model under the inferred population distribution and dashed lines are 10% and 90 % percentiles. The good quality of the fit gives an *a posteriori* rationale for the relevance of our value of V_0.

Supplementary Figure 3. Population fits of the breast xenograft data under different growth theories

A

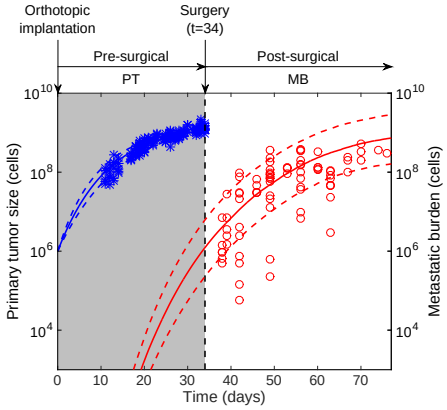

B

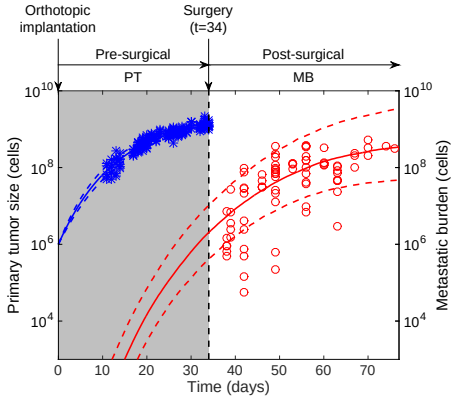

C

Model	Par.	Unit	Median value (CV)	NSE (%)
Diff growth alpha fixed	α_P	day^{-1}	0.605 (9.83)	3.57
	β_P	day^{-1}	0.0786 (12.2)	4.87
	μ	$cell^{-1} \cdot day^{-1}$	3.01e-09 (820)	72.4
	β	day^{-1}	0.0816 (15.7)	5.07
Same growth	α	day^{-1}	0.664 (16.3)	4.77
	β	day^{-1}	0.0893 (21.3)	6.22
	μ	$cell^{-1} \cdot day^{-1}$	4.43e-11 (176)	26.5
Diff growth Exp	α_P	day^{-1}	0.61 (9.88)	3.8
	β_P	day^{-1}	0.0796 (11.6)	5.09
	m	$mm^{-3} \cdot day^{-1}$	107 (3.55e+03)	62.4
	a	day^{-1}	0.114 (46.8)	11.7
Diff growth	α_P	day^{-1}	0.625 (11.4)	4.06
	β_P	day^{-1}	0.0822 (13.4)	5.31
	m	$cell^{-1} \cdot day^{-1}$	0.0075 (4.43e+04)	1.13e+06
	α	day^{-1}	1.29 (40.6)	54.7
	β	day^{-1}	0.071 (44.5)	36.7

Fits of the breast xenograft data under two models.
A: Same growth = same Gompertz growth parameters (α and β) for primary and secondary tumors.
B: Different growth alpha fixed = for each animal, same value of parameter α was imposed while value of β was allowed to vary between the PT and the secondary tumors.
C: Parameters estimates under the two different models.
With similar visual accuracy of the population fits (also observable in individual fits of particular mice, data not shown), the second model generated substantially higher uncertainty on the parameter estimation, especially parameter μ, with respective normalized standard errors (NSE) of 26.5% for the “same growth” model and 72.1% for the “different growth with alpha fixed” model. Additionally, probably due to sharper estimation of the parameters, predictive performances were improved with the “same growth” model (results not shown).

Supplementary Figure 4. Population fits of the kidney isograft data under different growth theories

A

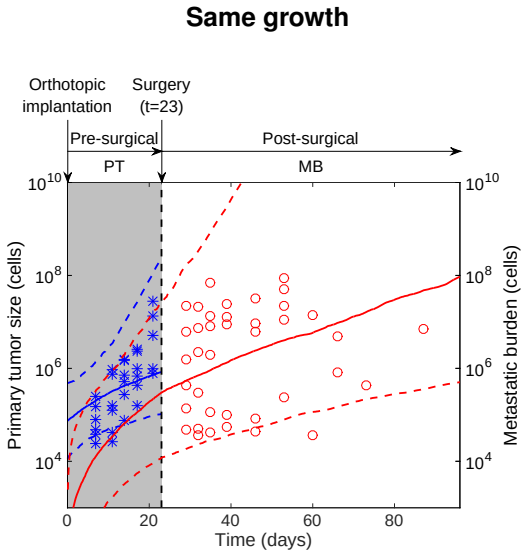

B

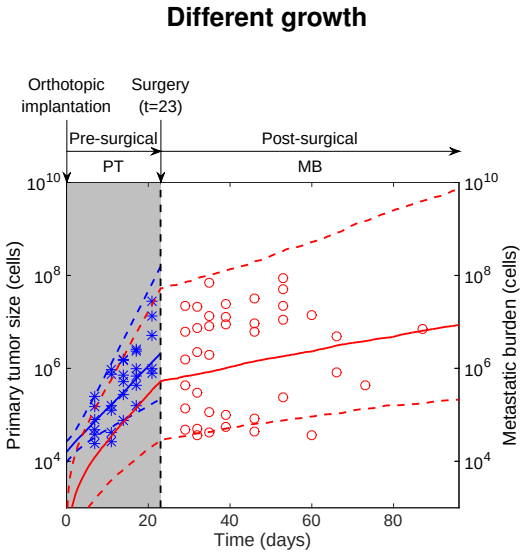

C

Model	Par.	Unit	Median value (CV)	NSE (%)
Diff growth exp	V_i	p/s	1.63e+05 (45.5)	29.9
	α_P	day^{-1}	0.21 (60.3)	17.2
	μ	$cell^{-1} \cdot day^{-1}$	0.00415 (397)	48.4
	α	day^{-1}	0.0307 (201)	48.9
Same growth exp	V_i	p/s	8.05e+05 (779)	53.7
	α	day^{-1}	0.0831 (325)	40.4
	μ	$cell^{-1} \cdot day^{-1}$	0.000892 (2.88e+03)	77.4

Fits of one of the datasets for the isograft kidney model (surgery at day 23) under two models for the growth of secondary tumors in relationship to the PT. At the structural level, both growths were considered exponential.
A: Same growth rate between primary and secondary tumors.
B: Different growth rate between primary and secondary tumors.
C: Parameters estimates under the two different models.
We chose the second model to be best adapted because: 1) the population fit was more accurate, especially for description of the inter-animal variability, 2) adding a parameter did not result in deterioration of the normalized standard errors (NSE) of the parameters estimates and 3) the low descriptive power of the “same growth” model was confirmed by a large inaccuracy in individual fits (results not shown)

Supplementary Figure 5. Second kidney data set used for fitting the data (resection time = 23 days)

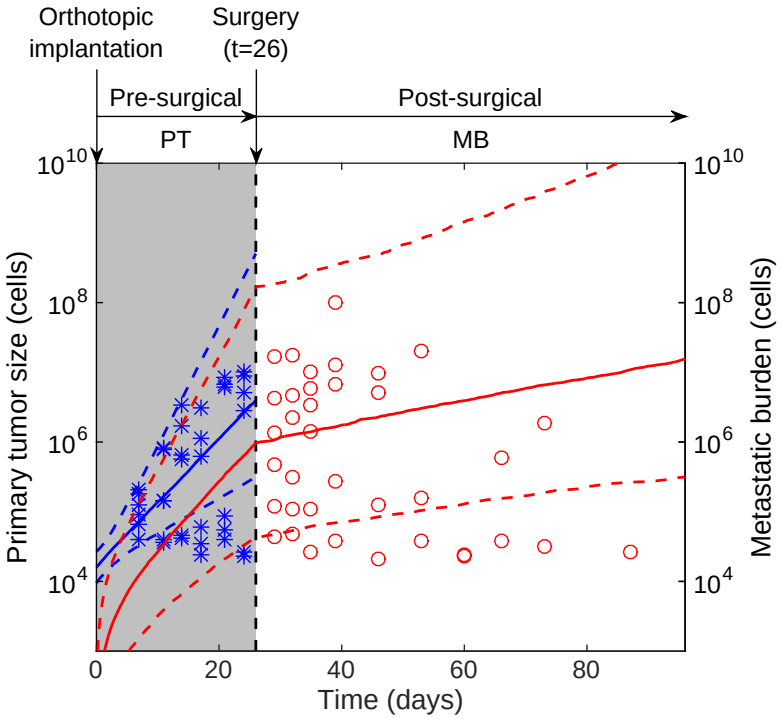

Supplementary Figure 6. Individual fits of primary tumor and metastatic burden kinetics. Breast animal model

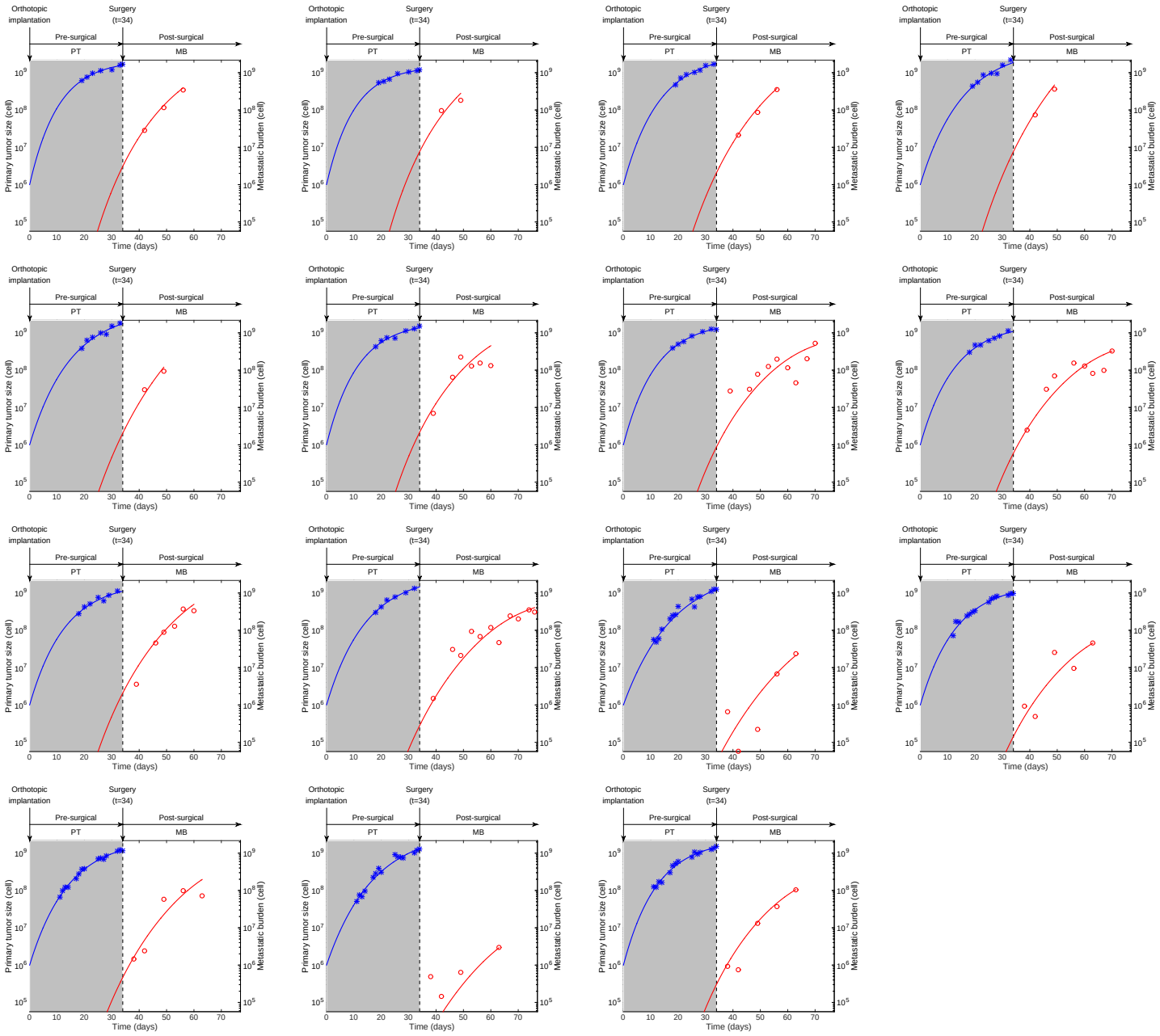

Equivalent of Figure 3 with all the animals. Each animal was fitted separately.

Supplementary Figure 7. Individual fits of primary tumor and metastatic burden kinetics. Kidney animal model

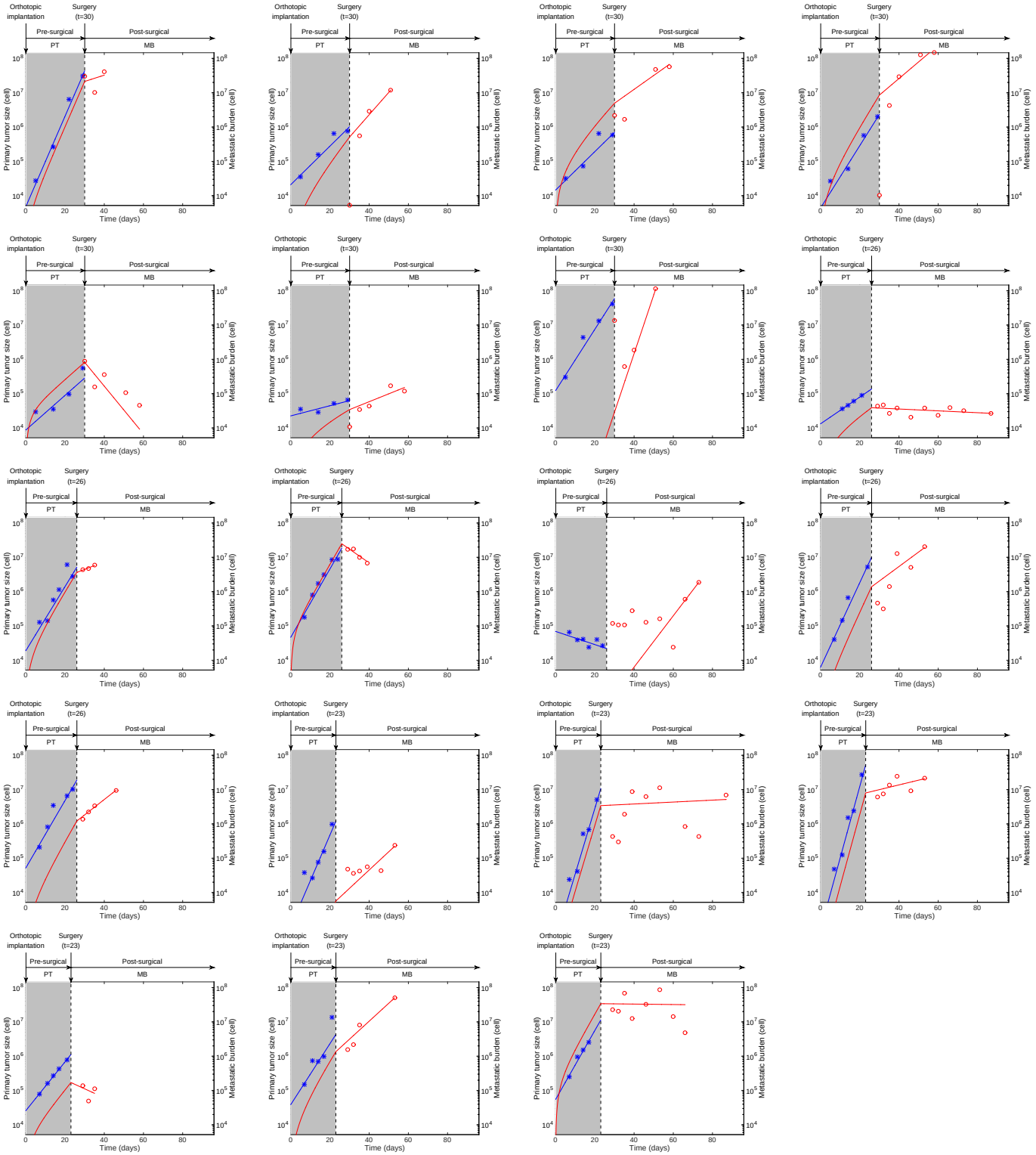

Equivalent of Figure 3 with all the animals. Each animal was fitted separately.

Supplementary Figure 8. Link between experimental and model survival

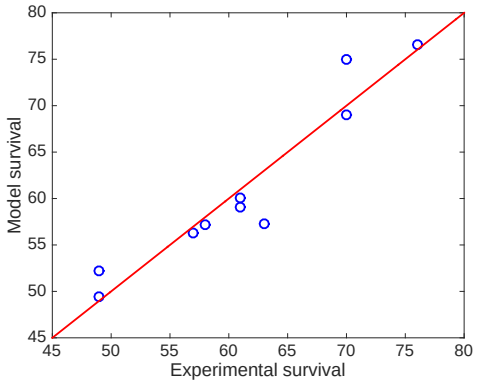

Predicted versus experimental survival. The model survival was defined as the time to reach a given lethal burden of $4 \cdot 10^9$ p/s, i.e. $\inf \left\{ t > 0; M(t) > 4 \cdot 10^9 \right\}$

Supplementary Figure 9: Surgery benefit on survival and metastatic burden reduction as a function of resection size, for varying values of metastatic potential (parameter μ)

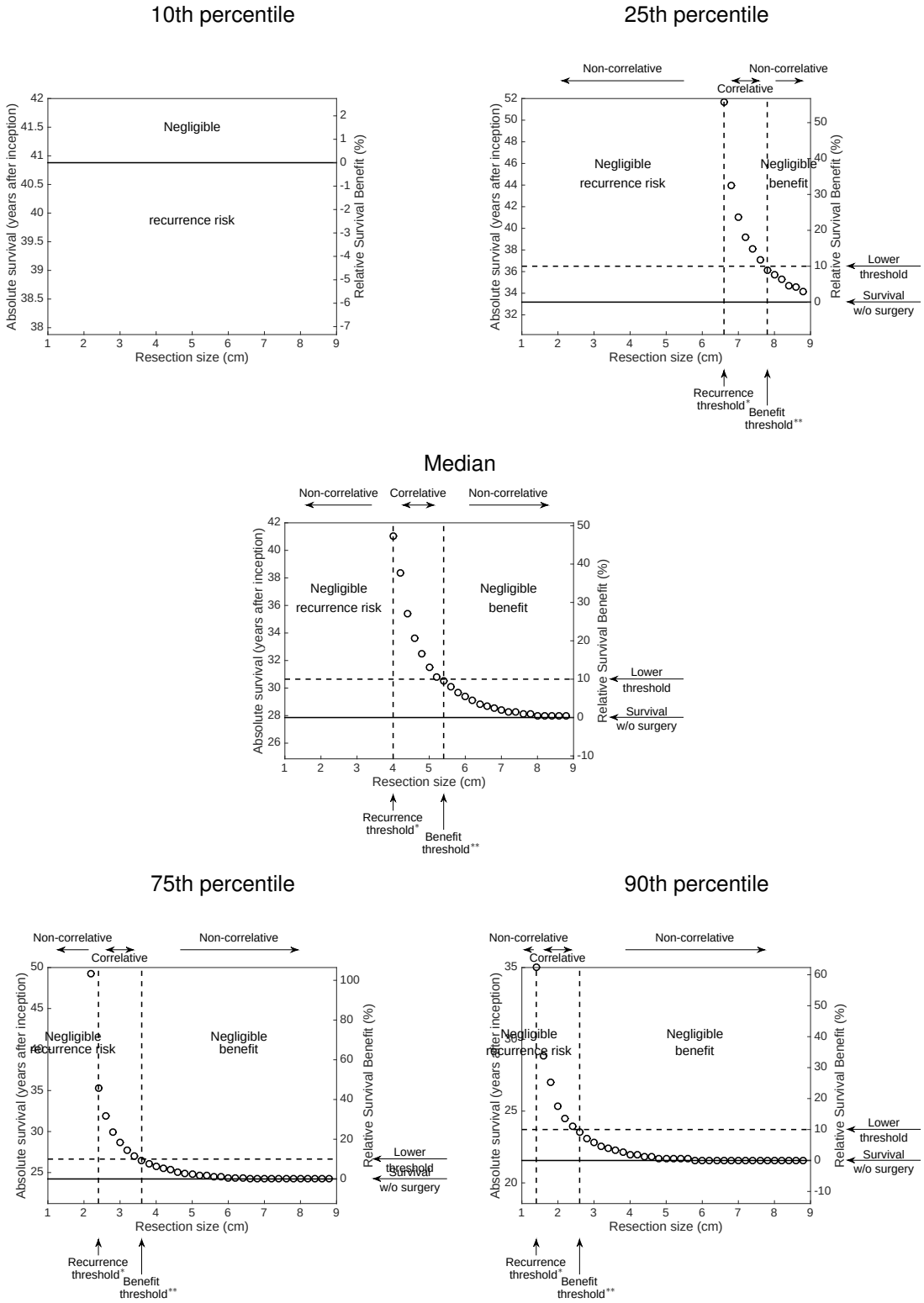

Supplementary Figure 10. Population fits of the ortho-surgical metastasis animal models for a dissemination coefficient $\mathrm{d}(\mathrm{V_p}) = \mu \mathrm{V_p^{\gamma}}$ and various values of γ

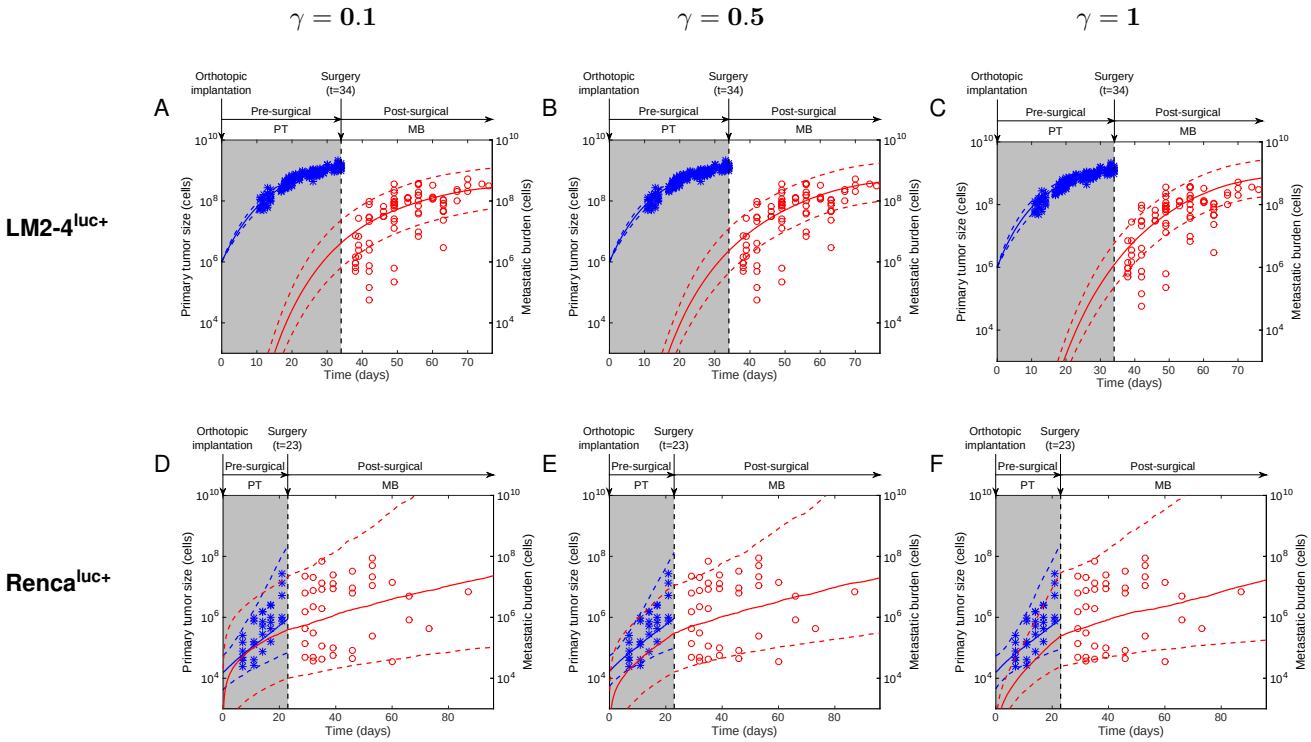

A - C: Xenograft breast model (LM2-4^{luc+})

D - E: Isograft kidney model (Renca^{luc+}). Only group with surgery at t = 23 days is shown.

Other intermediate values of γ between 0 and 1 produced similar, visually equivalent fits.

Supplementary Figure 11. Population fits of the ortho-surgical metastasis animal models for various values of the signal-to-cell ratio V_0

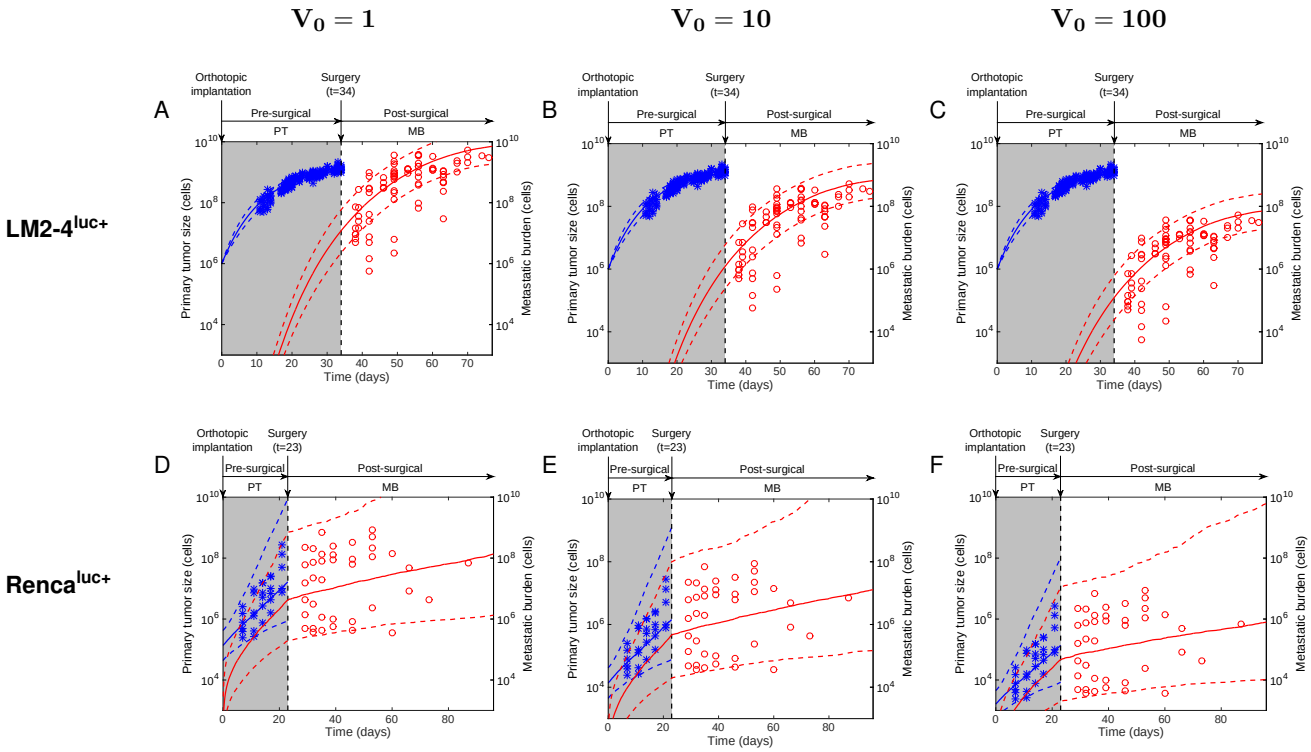

G

V_0 (p/s)	1.0	10.0	100.0
LM2-4^{luc+}	4.43×10^{-10}	4.16×10^{-11}	4.50×10^{-12}
Renca^{luc+}	0.0298	0.0348	0.0375

The relationship between BL and volume was far from perfectly linear in supplementary Figure 1B. This suggests that, for detectable volumes, the number of living tumor cells might not be proportional to the tumor volume, consistently with general laws of tumor growth (37). Hence, considering the relatively poor reliability of the extrapolated value of V_0, simulations were performed to test the robustness of the results with respect to the value of V_0, by varying V_0 over two orders of magnitude. Similar fits were obtained for the metastatic burden (MB) (supplementary Figure 10), showing that, for our concern here (the MB), different values of V_0 were virtually equivalent.

A - C: Xenograft breast model (LM2-4^{luc+})

D - E: Isograft kidney model (Renca^{luc+}). Only group with surgery at t = 23 days is shown.

Goodness-of-fit performances were the same for each value of V_0. The data is shifted along the y-axis because the conversion rule was used to convert the bioluminescence data into cell numbers. For the breast data, primary tumor volumes were measured in mm^3 using calipers and then converted into cell numbers using the conversion rule 1 mm$^3 \simeq 10^6$ cells. Hence, the conversion did not depend on V_0 and the data was not shifted when changing V_0.

G: Population estimate of μ (in cell$^{-1}\cdot$ day^{-1}) for the different values of V_0.

Supplementary Movie 1: Simulation of the cancer history from the first cancer cell for a virtual patient with median μ

Primary tumor (PT) was assumed to be detected when reaching the size of 4.32 cm in diameter. Post-diagnosis PT growth and development of metastases in the case of no surgical intervention are indicated as dashed line in the left plot and white bars in the histogram on the right, respectively.

Supplementary Movie 2: Simulation of the cancer history from the first cancer cell for a virtual patient with large μ, at the 90th percentile.

Primary tumor (PT) was assumed to be detected when reaching the size of 4.32 cm in diameter. Post-diagnosis PT growth and development of metastases in the case of no surgical intervention are indicated as dashed line in the left plot and white bars in the histogram on the right, respectively.

Supplementary text

Using the model from [Hartung et al., 2014] on the LM2-4^{luc+} data

In [Hartung et al., 2014], Hartung, Mollard et al. had developed a similar modeling analysis on data from breast cancer xenografts, however with no consideration of primary tumor surgery and in severely immune-incompetent mice. Thus, it could have been interesting to see whether the modeling analysis brings any insights on the differences between the cases with and without surgery. Unfortunately, quantitative comparison was hampered by the following points: different number of cells injected, different mice strain (severe combined immuno-deficient in our case versus Nod-scid gamma in their case), different bioluminescence quantification method (2D versus 3D) that resulted in a different cell-to-signal ratio and integration of peritoneal metastases for them versus only pulmonary metastases for us. Keeping all these flaws in mind, we nevertheless applied their model to our ortho-surgical data set of breast xenografts. This consisted in the use of a dissemination coefficient with the form $d(V_p) = \mu V_p^{2/3}$, different growth rates for the primary tumor and the metastases, and a different parameterization of the Gompertz growth rate, written as: $g(V) = aV \ln\left(\frac{b}{V}\right)$. We obtained a significantly larger value of a in our data of 4.91×10^{-2} day^{-1} $\pm\, 2.02 \times 10^{-3}$ versus 7.9×10^{-3} day^{-1} $\pm\, 2.5 \times 10^{-3}$ in [Hartung et al., 2014] (population estimate $\pm$ standard error). This could suggest post-surgery acceleration of metastases. On the other hand, the value of μ was also found significantly different, with several order of magnitudes of difference. We computed $\mu = 7.24 \times 10^{-3} \pm 8.5 \times 10^{-3}$ cell$^{-2/3}\cdot$ day^{-1} versus $\mu = 6.31 \times 10^{-1} \pm 4.42 \times 10^{-1}$ cell$^{-2/3}\cdot$ day^{-1} in [Hartung et al., 2014]. Indeed, it was already visible in the data without performing any quantitative analysis that they obtained a larger metastatic burden for smaller primary tumor sizes.

Supplementary methods

Preclinical methodology

Ortho-surgical models of metastasis

For ortho-surgical metastasis models, we followed detailed experimental criteria to control for variable disease progression and model standardization as previously described [Ebos et al., 2014]. For example, in breast (LM2-4^{LUC+}) and kidney (RENCA^{LUC+}) models, tumor invasion noted during surgery such as growth into peritoneal space (breast) or presentation of a non-encapsulated kidney tumor led to mouse exclusion from study. Additionally, if no tumor was present at any time before and after surgery (determined by bioluminescence or visible macroscopically), mice were excluded from study so as not to give potential false positive or negative bias to results (see [Ebos et al., 2014]). Note: all animals used in this study represent vehicle-treated controls from published [Ebos et al., 2014] and unpublished studies involving sunitinib malate. Therefore all animals in this study were treated with 10ml/kg vehicle for 7-14 days prior to tumor resection. Vehicle contained carboxymethylcellulose sodium (USP, 0.5% w/v), NaCl (USP, 1.8% w/v), Tween-80 (NF, 0.4% w/v), benzyl alcohol (NF, 0.9% w/v), and reverse osmosis deionized water (added to final volume) and adjusted to pH 6 (see [Ebos et al., 2008]). Importantly, no difference in metastatic disease progression patterns or survival has been observed between vehicle and untreated animals ([Ebos et al., 2014] and data not shown).

Bioluminescent imaging

Quantification of local and disseminated tumor burden by bioluminescent imaging has been previously described in detail (see [Ebos et al., 2014] and [Ebos et al., 2008]). Briefly, mice were injected intraperitoneally with substrate D-luciferin at 150 mg/kg in Dulbecco's

Phosphate Buffered Saline (Corning, Cat. #MT21-031-CV) and, after a 10 minute interval, anesthetized (4% isoflurane in oxygen for induction, 2% for maintenance) and placed onto the warmed stage inside the light-tight camera box (IVIS™ ; Xenogen, Alemeda, CA) as previously described ([Ebos et al., 2009] and [Ebos et al., 2014]). Light emitted from bioluminescent cells after 1 minute was detected by the IVIS® camera system with images quantified for tumor burden using a log-scale color range set at 5×10^4 to 1×10^7 and measurement of total photon counts per second (p/s) using Living Image software (Xenogen)

Mathematical methodology: Stochastic dynamics of metastasis formation

The formalism we employed to fit the model to the data was deterministic, because fast simulations were required for the large number of computations of the model needed for fitting the data. However, when considering simulation of individual dynamics (Figure 4), stochastic dynamics were simulated. The stochasticity here refers to intra-individual randomness in the metastatic dissemination. The stochastic version of the model was the following. The formation of new metastatic foci was assumed to be a sequence of random events exponentially distributed with rate $d(V_p(t))$. The number of metastases followed then a Poisson process $\mathcal{N}(t)$ with intensity $d(V_p(t))$. The appearance time of the i-th metastasis was defined by

$$T_i = \inf \{t \geq 0;\ N(t) \geq i\}$$

Adapting the methodology of [Iwata et al., 2000] to the case of randomly distributed dissemination times and denoting $\tilde{\rho}$ the resulting random size distribution of metastases, $\tilde{\rho}$ was a sum of Dirac masses solving the following problem

$$\begin{cases} \partial_t \tilde{\rho}(t,v) + \partial_v(\tilde{\rho}(t,v)g(v)) = 0 & t \in]0,+\infty[,\ v \in]V_0,+\infty[\\ g(V_0)\tilde{\rho}(t,V_0) = \sum_{i=1}^{+\infty} \delta\left(t = T_i\right) & t \in]0,+\infty[\\ \tilde{\rho}(0,v) = 0 & v \in]V_0,+\infty[\end{cases} \tag{1}$$

Equivalently, denoting by V_i the volume of the i-th metastasis, we have

$$\begin{cases} \frac{dV_i}{dt} = g(V_i(t)) \\ V_i(T_i) = V_0, \quad V_i(t) = 0, \text{ for } t \leq T_i \end{cases}$$

From these considerations the stochastic total metastatic burden at time t, denoted by $\mathcal{M}(t)$ was defined by

the following expression

$$\mathcal{M}(t) = \int_{V_0}^{+\infty} v\tilde{\rho}(t,v)dv = \sum_{i=1}^{+\infty} V_i(t)$$

The two approaches (deterministic and stochastic) are in fact closely and consistently linked. It can be shown [Hartung and Christophe, 2014] that the quantities $M(t)$ and $N(t)$ defined in the body text (section "quick guide to equations and assumptions") are the respective expectations of $\mathcal{M}(t)$ and $\mathcal{N}(t)$.

References

[Ebos et al., 2008] Ebos, J. M. L., Lee, C. R., Bogdanovic, E., Alami, J., Van Slyke, P., Francia, G., Xu, P., Mutsaers, A. J., Dumont, D. J., and Kerbel, R. S. (2008). Vascular endothelial growth factor-mediated decrease in plasma soluble vascular endothelial growth factor receptor-2 levels as a surrogate biomarker for tumor growth. *Cancer Res*, 68(2):521–529.

[Ebos et al., 2009] Ebos, J. M. L., Lee, C. R., Cruz-Munoz, W., Bjarnason, G. A., Christensen, J. G., and Kerbel, R. S. (2009). Accelerated metastasis after short-term treatment with a potent inhibitor of tumor angiogenesis. *Cancer Cell*, 15(3):232–239.

[Ebos et al., 2014] Ebos, J. M. L., Mastri, M., Lee, C. R., Tracz, A., Hudson, J. M., Attwood, K., Cruz-Munoz, W. R., Jedeszko, C., Burns, P., and Kerbel, R. S. (2014). Neoadjuvant antiangiogenic therapy reveals contrasts in primary and metastatic tumor efficacy. *EMBO Mol Med*, 6(12):1561–1576.

[Hartung and Christophe, 2014] Hartung, N. and Christophe, G. (2014). A stochastic framework for secondary metastatic emission.

[Hartung et al., 2014] Hartung, N., Mollard, S., Barbolosi, D., Benabdallah, A., Chapuisat, G., Henry, G., Giacometti, S., Iliadis, A., Ciccolini, J., Faivre, C., and Hubert, F. (2014). Mathematical modeling of tumor growth and metastatic spreading: validation in tumor-bearing mice. *Cancer Res*, 74(22):6397–6407.

[Iwata et al., 2000] Iwata, K., Kawasaki, K., and Shigesada, N. (2000). A Dynamical Model for the Growth and Size Distribution of Multiple Metastatic Tumors. *J Theor Biol*, 203(2):177–186.